Stability of Model Fe-Cr-Al Alloys Under The Presence of Neutron Radiation

Kevin G. Field
Xunxiang Hu
Ken Littrell
Yukinori Yamamoto
Richard Howard
Lance L. Snead

September 19th, 2014

OAK RIDGE NATIONAL LABORATORY
MANAGED BY UT-BATTELLE FOR THE US DEPARTMENT OF ENERGY

DOCUMENT AVAILABILITY

FCRD Advanced Fuels Campaign

Stability of Model Fe-Cr-Al Alloys Under the Presence of Neutron Radiation

Kevin G. Field
Xunxiang Hu
Ken Littrell
Yukinori Yamamoto
Richard Howard
Lance L. Snead

Date Published: Septmember 2014

CONTENTS

LIST OF FIGURES

LIST OF TABLES

ACRONYMS

ABF	Annular Bright Field
ADF	Annular Dark Field
AFC	Advanced Fuel Campaign
APT	Atom Probe Tomography
ATF	Accident Tolerant Fuel
bcc	Body Centered Cubic
BF	Bright Field
CBED	Convergent Beam Electron Diffraction
dpa	Displacements Per Atom
DOE	Department of Energy
FEG	Field Emission Gun
FIB	Focused Ion Beam
HFIR	High Flux Isotope Reactor
IMET	Irradiated Materials Examination and Testing
LAMDA	Low Activation Materials Development and Analysis
LEAP	Local Electrode Atom Probe
R&D	Research and Development
ODS	Oxide Dispersion Strengthened
ORNL	Oak Ridge National Laboratory
SANS	Small Angle Neutron Scattering
STEM	Scanning Transmission Electron Microscopy
TEM	Transmission Electron Microscopy
THT	Target Hydraulic Tube

ACKNOWLEDGMENTS

ABSTRACT

The iron based Fe-Cr-Al alloy system has the potential to form an important class of accident tolerant cladding materials in the nuclear power industry due to the alloy system exhibiting nearly three orders of magnitude higher oxidation resistance in high temperature steam environments compared to traditional Zr-based alloys. Past experience on ferritic Fe-Cr based alloys shows an as-irradiated microstructure evolution that includes dislocation loops, void/bubbles, and precipitation of second phases. These defects can significantly alter the mechanical properties at LWR-relevant irradiation conditions. However, the trends associated with the formation of these defects in Fe-Cr-Al alloys have not been fully established. Here, a series of Fe-Cr-Al alloys with 10-22 wt.% Cr and 2.9-4.9 wt.% Al were irradiated in the High Flux Isotope Reactor at 387 °C to 1.6 dpa to investigate the irradiation induced microstructural evolution as a function of alloy composition. Small angle neutron scattering and atom probe tomography was used to quantify the formation of Cr-rich α' precipitates, while scanning transmission electron microscopy was used to quantify the dislocation loop density and size. Results indicate precipitation of Cr-rich α' is dependent on the bulk Cr composition with the number density being most sensitive to Cr composition. Dislocation loops with Burgers vector of $a/2\langle 111\rangle$ and $a\langle 100\rangle$ were detected and quantified. Mechanical testing of sub-size-irradiated tensile specimens indicates the hardening response seen after irradiation is caused by the formation of these radiation-induced defects. A radiation induced hardening model was developed based on the dispersed barrier hardening model and indicated the change in yield strength after irradiation is dominated by the large number density of Cr-rich α' precipitates. Based on these results it is concluded that the stability of Fe-Cr-Al alloys in the presence of neutron irradiation is Cr composition dependent with reductions in Cr content significantly increasing the performance of the alloys after irradiation.

1. INTRODUCTION

The recent nuclear accident which occurred in Japan in 2011 has spawned a significant research thrust on the development of material systems for light water reactors (LWRs) which can withstand severe accident scenarios. This is due to the current fuel-clad systems in LWRs utilizing Zr-based alloys which are known to degrade above 1200 °C from oxidation in a steam environment. Such degradation leads to cladding consumption in accident scenarios such as loss of coolant accidents (LOCAs) [1, 2, 3]. Fe-based alloys have been selected as a potential replacement material for Zr-based clad to enhance the overall safety margins and accident tolerance of the current LWR fleet. Within this class of materials, is the sub-class of Fe-Cr-Al alloys with minor Y additions. Fe-Cr-Al alloys have indicated three orders of magnitude higher oxidation resistance in high temperature steam environments up to 1475 °C compared to Zr-based alloys [2].

Current research efforts have focused on developing wrought, nuclear grade Fe-Cr-Al alloys which balance the Cr and Al solute additions to optimize the aqueous corrosion and high temperature oxidation resistance while still maintaining acceptable properties for nuclear applications including formability, mechanical properties, weldability, neutronics and radiation tolerance [4, 5, 6]. Fe-Cr-Al alloys are being targeted as cladding material and therefore can expect a neutron radiation environment at temperatures in the vicinity of 300 °C depending on the LWR configuration. Such radiation environments have been known to degrade the mechanical performance of body centered cubic (*bcc*) Fe-Cr based alloys. Past experience on high-Cr, Fe based alloys for nuclear applications have shown the possibility of radiation induced hardening and embrittlement at temperatures relevant to nuclear fuel cladding applications [7].

The radiation induced hardening and embrittlement in the vicinity of 300 °C under irradiation has been attributed to the formation of dislocation loops and a phase instability in high-Cr (>8 wt. % Cr) alloys causing the formation of Cr-rich α' phases. The major contributing factors to the radiation induced hardening in binary Fe-Cr alloys has been shown to be, at least in part, Cr composition dependent. For example, a recent review by Terentyev *et al.* [8] has shown above ~8 wt. % Cr the hardening and embrittlement response is due to the formation of the Cr-rich α' phase with minor contributions due to dislocation loop formation. Below ~8 wt. % Cr, the hardening response is solely dominated by dislocation loop formation as the alloys with lower Cr content are not within the two phase $\alpha - \alpha$' regime. The formation of dislocation loops in *bcc* Fe-Cr alloys is due to the coalescing of mobile interstitial atoms generated from the damage cascade and quench.

The formation of Cr-rich α' has been demonstrated in a wide range of alloys through simple thermal aging studies. The formation can cause serve hardening and embrittlement; this effect is historically known as the "475 °C embrittlement" in non-irradiated materials. For irradiated materials, the formation of α' has been observed below the peak thermal aging temperature of 475 °C and it is believed this acceleration is due to the production of mobile point defects after the damage cascade and quench enhancing Cr redistribution [9, 10, 11]. Bonny *et al.* [10] reviewed the literature on Cr bearing Fe based alloys and showed α' formation under irradiation is a function of both temperature and Cr content for model, complex, and commercial Fe-Cr alloys. Within this review, no Fe-Cr-Al based alloys were investigated. Published works have also indicated thermal annealing in Fe-Cr-Al alloys can lead to α' formation [12, 13, 14]. It is therefore reasonable to expect the possibility of α' formation in Fe-Cr-Al alloys after irradiations conducted in the vicinity of 300 °C.

To reach commercialization of Fe-Cr-Al alloys for the nuclear industry, it is necessary to demonstrate the microstructural stability of the alloys and mechanical properties in the presence of a neutron environment. This work focuses on understanding the Cr and Al composition dependence on the the microstructural evolution and mechanical properties of Fe-Cr-Al alloys after neutron irradiation in the High Flux Isotope Reactor (HFIR). The dislocation loop morphology and phase stability after irradiation below 400 °C was characterized using advanced characterization techniques including scanning transmission electron microscopy (STEM), small angle neutron scattering (SANS), and atom probe tomography (APT). In parallel to the characterization studies, the mechanical properties were investigated using sub-sized tensile specimens and related to the changes in microstructure through a simplified radiation induced hardening model for the four model Fe-Cr-Al alloys.

2. MATERIALS AND METHODS

2.1 MATERIALS

Model and commercial Fe-Cr-Al alloys with varying Al and Cr composition were utilized for this study. The nominal Cr content was varied between 10 and 22 wt. % Cr in the model alloys. The chemical composition of each model alloy studied can be found in Table 1. Y was added to increase the oxidation resistance at elevated temperatures as Y is known to reduce the growth rate and increase adherence of protective, external alumna scale in Fe-Cr-Al alloys [15, 16]. Model alloys were fabricated by arc-melting pure element feed stocks and pre-alloyed Al-Y specimens. After arc-melting the model alloys were hot forged/rolled and heat treated to control the grain size to 20-50 μm. Cold rolling with a 10% thickness reduction was used to flatten the sheet samples prior to machining. The as-received microstructure can be seen in Figure 1 for all model alloys. Two commercial alloys, Kanthal APMT and K720 were also selected. The compositions of the commercial alloys are also provided in Table 1.

SS-J2 tensile specimens were machined using electric discharge machining (EDM) to final dimensions. The dimensions of the SS-J2 specimens are given in Figure 2. The SS-J2 specimens were irradiated in the target hydraulic tube (THT) facility of the HFIR. The neutron irradiated fluence was estimated at 1.83×10^{21} n/cm^2 (E > 0.1 MeV) corresponding to a nominal dose level of 1.6 dpa and a dose rate of 7.2×10^{-7} dpa/s. Target irradiation temperature was 320 °C.

At the time of reporting, the full characterization and mechanical testing of the commercial alloys was not completed. Therefore, the remaining sections of the report pertains only to the four model alloys listed in Table 1. Future work and reporting will include details on the commercial alloys to determine the effects of minor alloying additions on the radiation response of Fe-Cr-Al alloys.

Table 1. Summary of alloy compositions in wt. %

Alloy:	Fe-10Cr-4.8Al	Fe-12Cr-4.4	Fe-15Cr-3.9Al	Fe-18Cr-2.9Al	K720	APMT
Fe	85.15	83.56	80.99	79.52	81.36	69.01
Cr	**10.01**	**11.96**	**15.03**	**17.51**	**12.95**	**21.64**
Al	4.78	4.42	3.92	2.93	4.21	4.93
Y	0.038	0.027	0.035	0.017	0.0003	0.12
C	0.005	0.005	0.005	0.005	0.0342	0.03
S	0.0013	0.0013	0.0004	0.0006	0.0015	<0.001
O	0.0013	0.0017	0.0025	0.0015	0.0018	0.0494
N	0.0003	0.0009	0.0007	0.0011	0.0074	0.0504
P	0.006	0.004	<0.002	<0.002	0.008	0.01
Si	<.01	0.01	0.01	<0.01	0.3	<0.001
W	<.01	<0.01	<0.01	<0.01	<0.01	<0.01
Ce	<.01	<0.01	<0.01	<0.01	<0.01	<0.01
Co	<0.01	<0.01	<0.01	<0.01	0.02	0.02
Cu	<0.01	<0.01	<0.01	<0.01	0.01	0.04
Hf	<0.01	<0.01	<0.01	<0.01	<0.01	0.16
La	<0.01	<0.01	<0.01	<0.01	<0.01	<0.01
Mn	<0.01	<0.01	<0.01	<0.01	0.44	0.1
Mo	<0.01	<0.01	<0.01	<0.01	<0.01	2.77
Nb	<0.01	<0.01	<0.01	<0.01	<0.01	0.02
Ni	<0.01	<0.01	<0.01	<0.01	0.12	0.12
Ti	<0.01	<0.01	<0.01	<0.01	0.44	0.02
V	<0.01	<0.01	<0.01	<0.01	0.03	0.04
Zr	<0.01	<0.01	<0.01	<0.01	0.06	0.1
B	0.0007	0.0003	<0.0003	<0.0003	<0.0003	<0.0003
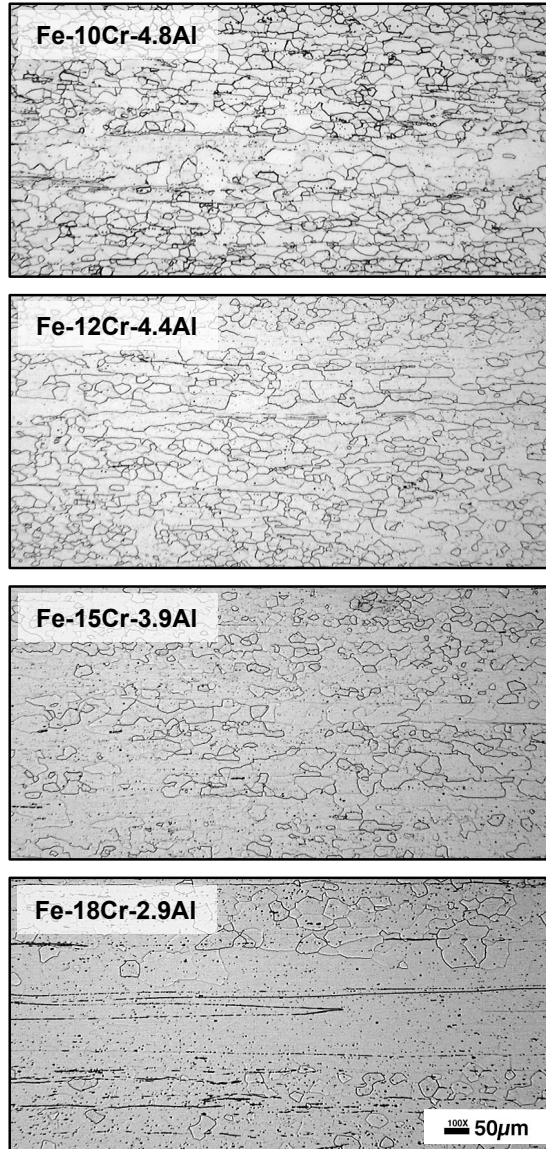
Fig. 1. Optical micrographs of model FeCrAl alloys showing grain structure.
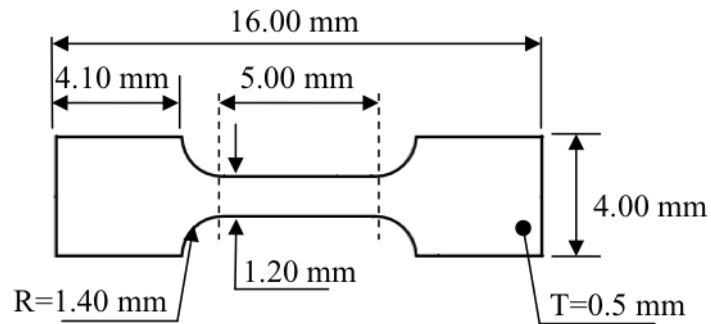
Fig. 2. SS-J2 tensile specimen used for HFIR irradiation.

2.2 SILICON CARBIDE THERMOMETRY

Passive SiC thermometry was utilized to determine the nominal temperature of the irradiation. Dilatometric analysis of the SiC passive temperature monitors was utilized. The dilatometry was conducted up to 600 °C at a constant ramp rate of 1 °C/min using a Netzsch 402 CD dilatometer. Typical data from the dilatometric analysis can be found in Figure 3. Three SiC passive temperature monitors were run to provide a statistical mean of the nominal irradiation temperature. Standard evaluations of SiC thermometry data can be prone to user bias to determine the inflection points in the fractional change data. Here, a smoothing function was applied to the fractional change between the heating and cooling curves from the dilatometric analysis. To obtain the nominal irradiation temperature, the maximum of the first derivative and second derivative was taken from the smoothed curve and then the tangent of the first derivative and second derivative were computed. Based on the intersection of the tangent of the points, the nominal temperature was calculated. This is shown as the green lines intersecting and the red dashed drop line in Figure 3. The computed average nominal irradiation temperature of the capsule irradiated in the THT facility was 386.7 ± 5.5 °C.
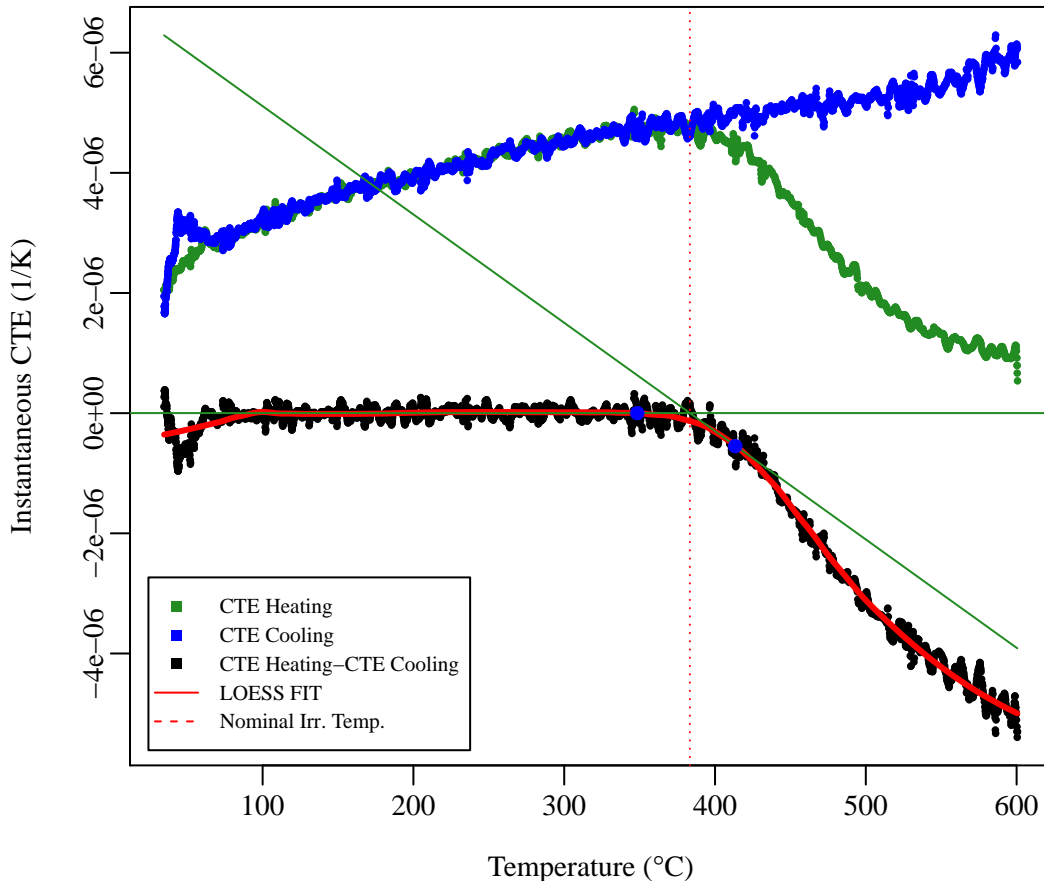
Fig. 3. Fractional change in the length of SiC thermometry and corresponding analysis.

6

2.3   MECHANICAL TESTS

Tensile tests were conducted using shoulder loading at a crosshead speed of 0.0055 mm/s corresponding to a strain rate of $\sim 10^{-3}$ s^{-1} on a screw-driven machine. The engineering strain was calculated from the recorded crosshead separation using the initial gauge length of 5.0 mm. The engineering stress was calculated by dividing the applied load by the initial cross sectional area. All tensile tests were performed at room temperature in the Irradiated Material Examination Testing (IMET) facility at Oak Ridge National Laboratory (ORNL).

2.4   TRANSMISSION AND SCANNING TRANSMISSION ELECTRON MICROSCOPY

Samples for electron microscopy and atom probe tomography (APT) were manufactured from broken tensile heads which had been mechanically polished to mirror finish using standard metallography techniques. Samples for transmission electron microscopy (TEM) and scanning transmission electron microscopy (STEM) were manufactured using standard FIB lift-out techniques on a FEI Quanta 3D 200i. FIB preparation was utilized to minimize magnetic aberrations [17] observed during TEM/STEM analysis due to the magnetic nature of the alloys investigated. Care was taken during sample preparation to minimize artificating due to FIB induced damage. All specimens were thinned to electron transparency using a 5 kV Ga^+ ion beam and cleaned with a 2 kV Ga^+ ion beam.

At least two FIB specimens were prepared from each irradiated alloy; any specimen showing inconsistent artificating under TEM investigation from FIB induced damage were excluded from further analysis. STEM and TEM was conducted at Oak Ridge National Laboratory (ORNL) using a Philips CM200 FEG-(S)TEM operating at 200 kV. Dislocation loop character was determined using annular bright field (ABF) on-zone STEM imaging with the grain of interest tilted to the [100] zone axis. More details on the conditions used for dislocation imaging and principles can be found in Section 3.1.1. Foil thickness was determined using convergent beam electron diffraction (CBED) analysis [18].

2.5   ATOM PROBE TOMOGRAPHY

Initially, APT samples were prepared by electropolishing using standard double layer and micropolishing techniques but the large volume size resulted in high sample activity and swamped the detector preventing accurate APT analysis. Therefore, specimens for APT were fabricated from the broken tensile heads using a FEI Quanta 3D 200i FIB which significantly reduced the volume size which in-turn reduced the background signal due to the activity of the specimens. APT was performed at ORNL using the Cameca Instruements local electrode atom probe (LEAP®) 4000X HR. APT was performed using laser mode with the specimen cooled to 30 K with a pulse repetition rate of 100 kHz. Phase separation was analyzed using standard APT analysis tools.

2.6   SMALL ANGLE NEUTRON SCATTERING

Small angle neutron scattering (SANS) was performed at ORNL on CG-2 general purpose beam-line at the HFIR [19]. The data were measured in 3 detector settings—sample to detector distance of 1.079 m and 7.779 m using 4.72 Å (0.472 nm) neutrons and 19.279 m using 12 Å (1.2 nm) neutrons—with the detector laterally offset by 0.4 m to maximize the accessible range of momentum transfer, Q, in each setting. The three settings together spanned the range 0.001<Q<1 Å^{-1} (0.01<Q<10 nm^{-1}). The data were placed on the cm^{-1} absolute scale by normalizing the medium data to the attenuated direct beam after correction for

thickness and transmission. Data in the other two settings were scaled to match the medium data to generate the combined curves. All measurements were performed at room temperature. Measurements were performed on broken tensile heads with a nominal thickness of 0.5 mm. Multiple scattering corrections were negligible. Analysis assumed nano-precipitates were Cr-rich α' with a nominal composition of Fe-82.2Cr-3.45Al (at.%) [13] and were spheres interacting with an exclusion volume.

3. RESULTS AND DISCUSSION

3.1   DISLOCATION LOOP FORMATION

3.1.1   Application of on-zone scanning transmission electron microscopy (STEM) imaging

Radiation induced hardening and embrittlement in structural materials has been attributed to dislocation loop formation under the presence of irradiation, particularly at temperatures near one-third of the melting temperature of the alloy [7]. The formation of these loops has been attributed to mobile point defects created from the damage cascade and quench coalescing to form extended length defects including dislocation loops. For bcc Fe and bcc Fe-Cr alloys it is generally accepted two types of dislocation loops can form: $b = a/2 \langle 111 \rangle$ and $b = a \langle 100 \rangle$ dislocation loops [20]. The ratio of $a/2 \langle 111 \rangle$ and $a \langle 100 \rangle$ loops have been reported to be dependent on the irradiation dose, temperature, and Cr content for an alloy of interest [21]. The variation in the ratio of different dislocation loop types can be partially attributed to the mobility of the two dislocation loop types, $a/2 \langle 111 \rangle$ loops are glissile (mobile) while $a \langle 100 \rangle$ loops are sessile (immobile) at temperatures relevant to cladding and structural material applications [22, 23]. Such mobility also has more global impacts on the material properties and could significantly impact the radiation induced hardening observed in bcc Fe and bcc Fe-Cr alloys. It is reasonable to expect that Fe-Cr-Al alloys will exhibit dislocation loops of the same morphology under irradiation as bcc Fe and bcc Fe-Cr alloys exhibit the same ferritic microstructure as those seen in the Fe-Cr-Al model alloys used in this study.

The dislocation loop morphology, size, and number density has typically been investigated using conventional transmission electron microscopy (CTEM). These studies require a series of image sequences on the same area of interest using different diffraction vectors, g, to satisfy the varying g·b invisibility criterion of the two different dislocation types and possible habit planes of each type. Such task is non-trivial for the novice microscopist and remains a labor-intensive task, even for the most veteran of microscopist. Recent work by Yao *et al.* [20] has sought to aid in such a task by using the g·b invisibility criterion and crystallographic information of bcc materials to publish the expected dislocation loop morphologies to be viewed on the viewing screen (or camera) for any given selected g vector. Such analysis is highly beneficial to quantify the density and density anisotropy of dislocation loops in bcc alloys but still requires a careful tilt-series to fully characterize a single region of interest within a TEM sample and can be prone to errors due to misinterpretation of the contrast observed in images.

Such issues with dislocation analysis using CTEM are not a singularity to irradiated materials. As such, an interest in the application of scanning transmission electron microscopy (STEM) using bright field (BF), annular bright field (ABF), or annular dark field (ADF) to image dislocation networks in unirradiated materials has grown [24, 25, 26, 27, 28]. The reason for such interest is STEM significantly reduces the elastic contrast in the background due to an averaging effect, it can be performed on thicker samples, and the traditional g·b invisibility criterion can remain applicable. Furthermore, the imaging in STEM and CTEM are equivalent due to reciprocity when imaging conditions in both modes are carefully selected. Finally, dislocations exhibit strong contrast due to de-channeling contrast and diffuse scattering [25, 27]. A recent publication by Phillips *et al.* [28] has reviewed the STEM based imaging of dislocations in unirradiated material. Of particular interest for irradiated bcc materials is on-zone STEM imaging.

By applying the imaging morphologies detailed by Yao *et al.* for two-beam CTEM imaging and the

principles of reciprocity for TEM and STEM, it becomes clear the application of on-zone STEM imaging can be used to easily image dislocation loops in irradiated *bcc* Fe and *bcc* Fe-Cr alloys. An example of the application of such technique is shown in Figure 4. Figure 4 shows dislocation loops formed in the irradiated Fe-15Cr-3.9Al model alloy imaged on the [100] zone axis in both CTEM-BF and STEM-ABF modes. Imaging down the [100] zone axis results in $a\langle 100\rangle$ loops to appear edge-on aligned with the [002] directions on the camera while $a/2\langle 111\rangle$ loops appear as elongated ellipses aligned with the [011] directions. Due to on-zone STEM simultaneously imaging all possible diffraction vectors for the [001] zone axis, as well as the relaxation of the g·b invisibility criterion allowing for faint contrast from in-plane a[100](200) loops, all possible dislocations morphologies, including line dislocations, can be imaged in a *single* micrograph. It should be noted such statements only hold true for those dislocation morphologies solely composed of line and loop dislocations with Burgers vectors of $a/2\langle 111\rangle$ and/or $a\langle 100\rangle$ in a *bcc* matrix. The application of such technique can be extended to image the line dislocation morphology in as-cast and cold worked material as line dislocations are anticipated to have the same Burgers vector as the dislocation loops formed after irradiation. The application of on-zone STEM based dislocation analysis was used in this study due to broad benefits of the technique over CTEM techniques.
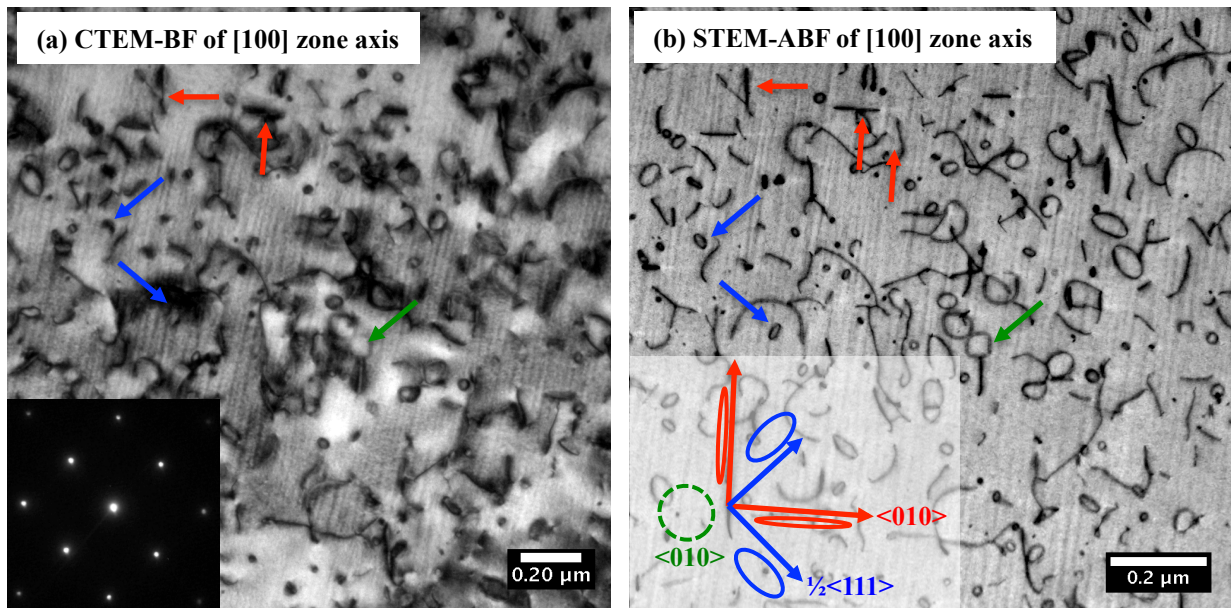
Fig. 4. Dislocation loop imaging using (a) CTEM and (b) STEM-ABF of dislocation loops in neutron irradiated model Fe-15Cr-3.9Al alloy. Inset in (a) shows TEM acquired [100] zone axis diffraction pattern. Inset in (b) shows expected dislocation loop morphologies. ($\langle 100\rangle$ type loops highlighted with red arrows, in-plane with a green arrow, and $a/2\langle 111\rangle$ loops highlighted with blue arrows)

3.1.2 As-received dislocation microstructure

The as-received microstructures were investigated using on-zone STEM based defect imaging described in Section 3.1.1. Figure 5 shows the dislocation microstructure before irradiation for all four model alloys investigated. The dislocation structure represented numerous dislocations organized in a pronounced cell

structure in all alloys, as expected from cold worked material. The dislocation density in the alloys varied from $7.2\pm2.2\times10^{13}$ m^{-2} to $1.6\pm0.4\times10^{14}$ m^{-2} depending on the alloy investigated. The Fe-10Cr-4.8Al alloy exhibited the lowest dislocation density of all alloys investigated. A limited number of grains were investigated per condition due to the small sample size ($\sim10\times10\times0.1$ μm) produced via FIB and the grain sizes being on the order of 20-50 μm. Several specimens showed large precipitates on the order of <1 μm in size but the chemical nature or structure of these precipitates were not investigated due to the limited number available for statistical characterization.
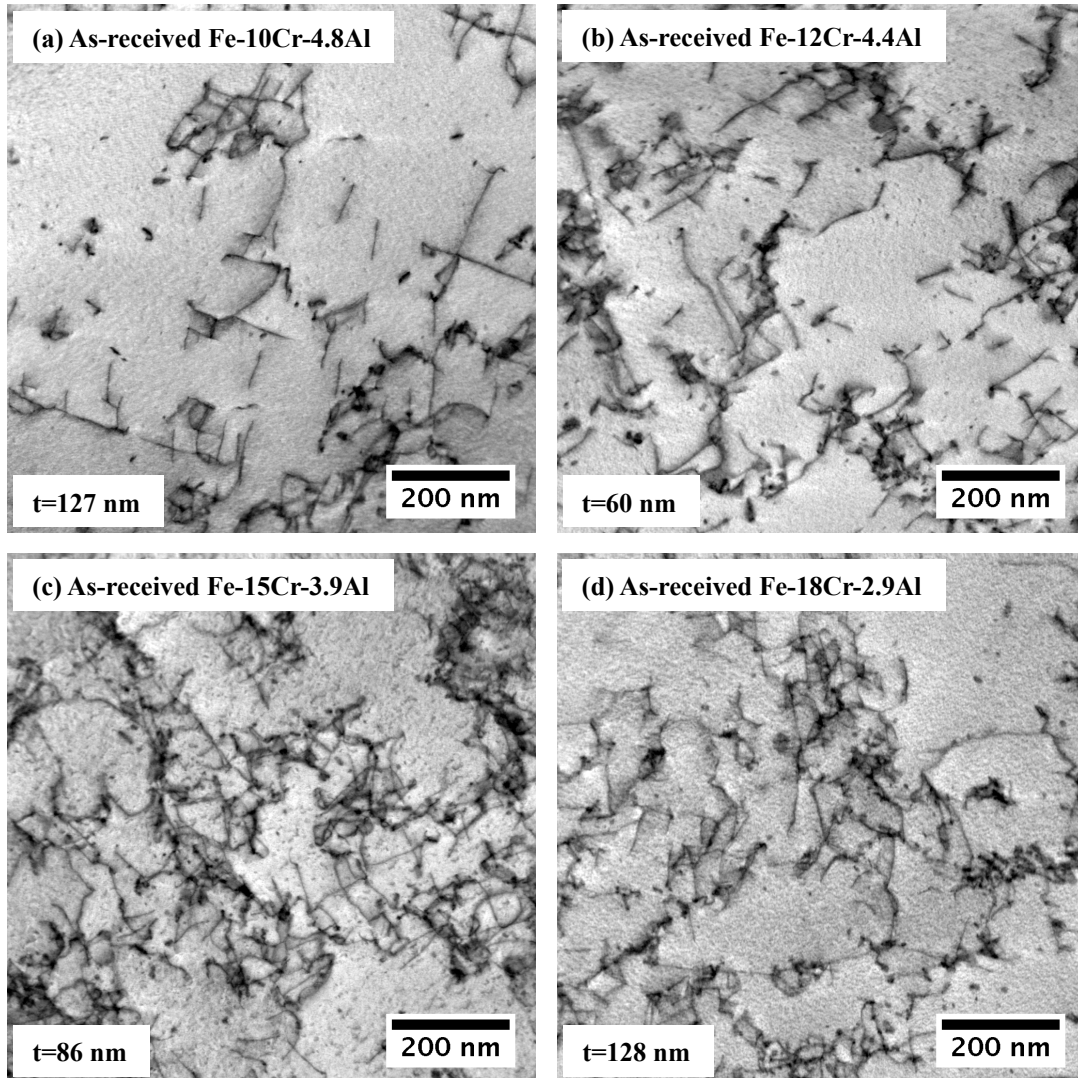
Fig. 5. Dislocation structure in unirradiated (a) Fe-10Cr-4.8Al, (b) Fe-12Cr-4.4Al, (c) Fe-15Cr-3.9Al, and (d) Fe-18Cr-2.9Al. STEM-ABF tilted to the [100] zone axis used to image dislocation structures. Measured foil thickness (t) using CBED analysis reported for reference.

3.1.3   Post-irradiation dislocation microstructure

All irradiated samples exhibited a microstructure containing dislocation loops of high number density with a sparse dislocation network. All samples investigated had a mixed population of $a/2\langle 111\rangle$ and $a\langle 100\rangle$ dislocation loops with the size, number density and loop anisotropy varying between alloys. Figure 6 shows typical micrographs of the dislocation microstructure in the irradiated specimens using STEM based defect imaging. It should be noted no evidence of voids or bubbles were observed in any of the specimens investigated at this irradiation dose and temperature. The absence of voids in the defect structure is expected, as Little and Stow [29] showed a Fe-14Cr-4Al alloy irradiated to 23 dpa between the temperatures of 380 °C and 615 °C exhibited no void swelling response within the detection limits of their system. The lack of voids/bubbles observed here and the result of Little and Stow indicates that Al additions in the ferritic Fe-Cr structure does not detrimentally impact the excellent swelling resistance of *bcc* Fe based alloys.

As seen in Figure 6, the dislocation microstructure also consisted of 'black dots'. Several specimens exhibited a significantly higher fraction of 'black dots' compared to the entire population of samples investigated. 'Black dot' damage has been observed in neutron irradiated steels but has also been attributed to artificating from FIB sample preparation [30]. It is believed the samples with a significantly higher fraction of 'black dots' is the superposition of both neutron radiation induced 'black dots' and artificating from the FIB and were not characterized. Those samples which exhibited 'black dot' damage inline with the population majority were considered real and characterized accordingly.

The dislocation structure was quantified to determine the size and number density for each dislocation type and hence dislocation anisotropy as a function of alloy content. The defect distributions in the irradiated specimens can be seen in Figure 7 for the model Fe-Cr-Al alloys. The $a/2\langle 111\rangle$ and $a\langle 100\rangle$ dislocation loops for all investigated alloys displayed a Gamma distribution based size distribution. As can be seen in Figure 7, few loops were characterized below ~10 nm while a majority of the 'black dots' existed below ~10 nm. Such distributions are most likely due to STEM based analysis technique incapable of uniquely identifying loops below the 10 nm cut-off, although further work would be needed to verify such assumptions. The size and number of characterized 'black dots' were nearly identical for all alloys with the average size between 8.2 and 9.8 nm and the average number density between $1.4\pm 0.4\mathrm{x}10^{20}$ m^{-3} and $1.6\pm 0.5\mathrm{x}10^{21}$ m^{-3}. The only alloy which showed a significant variation from the majority population was the Fe-12Cr-4.4Al alloy. The Fe-12Cr-4.4Al microstructure varied significantly from the other alloys with pronounced sub-grain boundaries and moderate dislocation cell networking. Only a limited number of field of views were analyzed for the Fe-12Cr-4.4Al alloy and therefore it is unclear as to whether the observed dislocation microstructure was atypical. Several factors could contribute to the anomalies in the sample such as variations in the temperature distribution along and across the irradiation capsule resulting in a irradiation temperature variance compared to the calculated nominal irradiation temperature. As such, the Fe-12Cr-4.4Al specimen is eliminated from further discussions about the change in dislocation microstructure as a function of alloying content.

With increasing Cr content and decreasing Al content for the Fe-10Cr-4.8Al, Fe-15Cr-3.9Al, and Fe-18Cr-2.9Al specimens, the size of $a/2\langle 111\rangle$ dislocation loops did not change significantly within the error of the analysis while the $a\langle 100\rangle$ dislocation loops decreased in size by nearly a 60% reduction. Such size changes are observable in the micrographs in Figure 6. In regards to dislocation loop density with increasing Cr content, the number density of $a/2\langle 111\rangle$ dislocation loops slightly increased from

1.7±0.7x10^{20} m^{-3} to 8.4±3.3x10^{20} m^{-3} while the density of $a\langle 100\rangle$ dislocation loops increased more with the Fe-10Cr-4.8Al specimen having a density of 4.7±2.4x10^{19} m^{-3} compared to the Fe-18Cr-2.9Al alloy having a density of 2.3.±0.9x10^{20} m^{-3}. As such, the ratio of $^{a}/_{2}\langle 111\rangle$ to $a\langle 100\rangle$ loops only changed slightly with increasing Cr content; the Fe-10Cr-4.8Al alloy had a ratio of 3.62 compared to the Fe-18Cr-2.9Al ratio of 3.65. The large grain sizes promoted a nearly uniform distribution of loops through the matrix for all alloys. No influence of the grain boundaries on the loop behavior was observed. The changes in the defect size and distributions suggest a possible link between the Cr concentration of Fe-Cr-Al alloys and the extended defect formation although further work is needed to conclusively determine any affects.
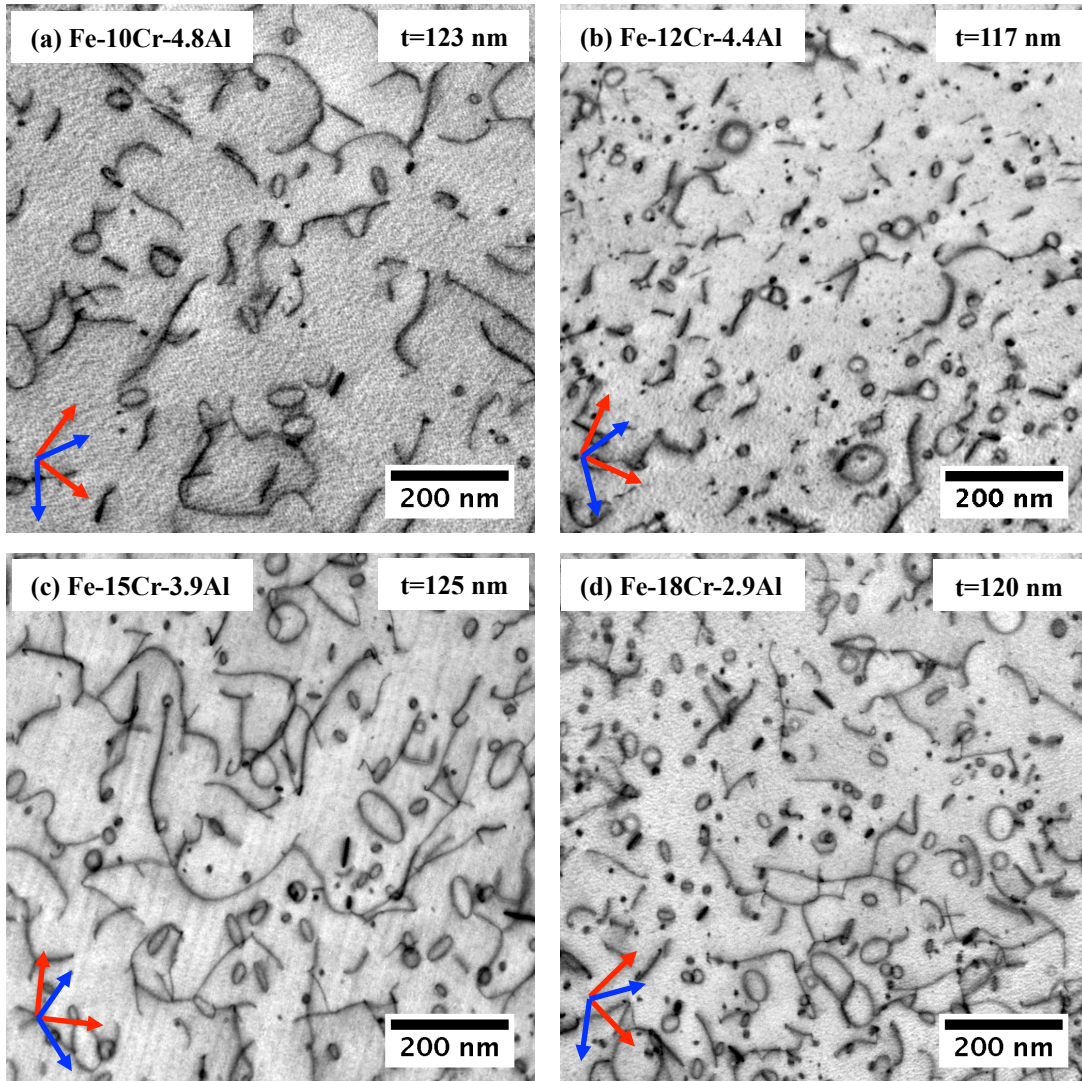
Fig. 6. Dislocation structure in irradiated (a) Fe-10Cr-4.8Al, (b) Fe-12Cr-4.4Al, (c) Fe-15Cr-3.9Al, and (d) Fe-18Cr-2.9Al. STEM-ABF tilted to the [100] zone axis used to image dislocation structures. Red arrows indicate the [002] directions while blue arrows indicate the [011] directions; for dislocation morphologies reference inset in Figure 4b. Measured foil thickness (t) using CBED analysis reported for reference.
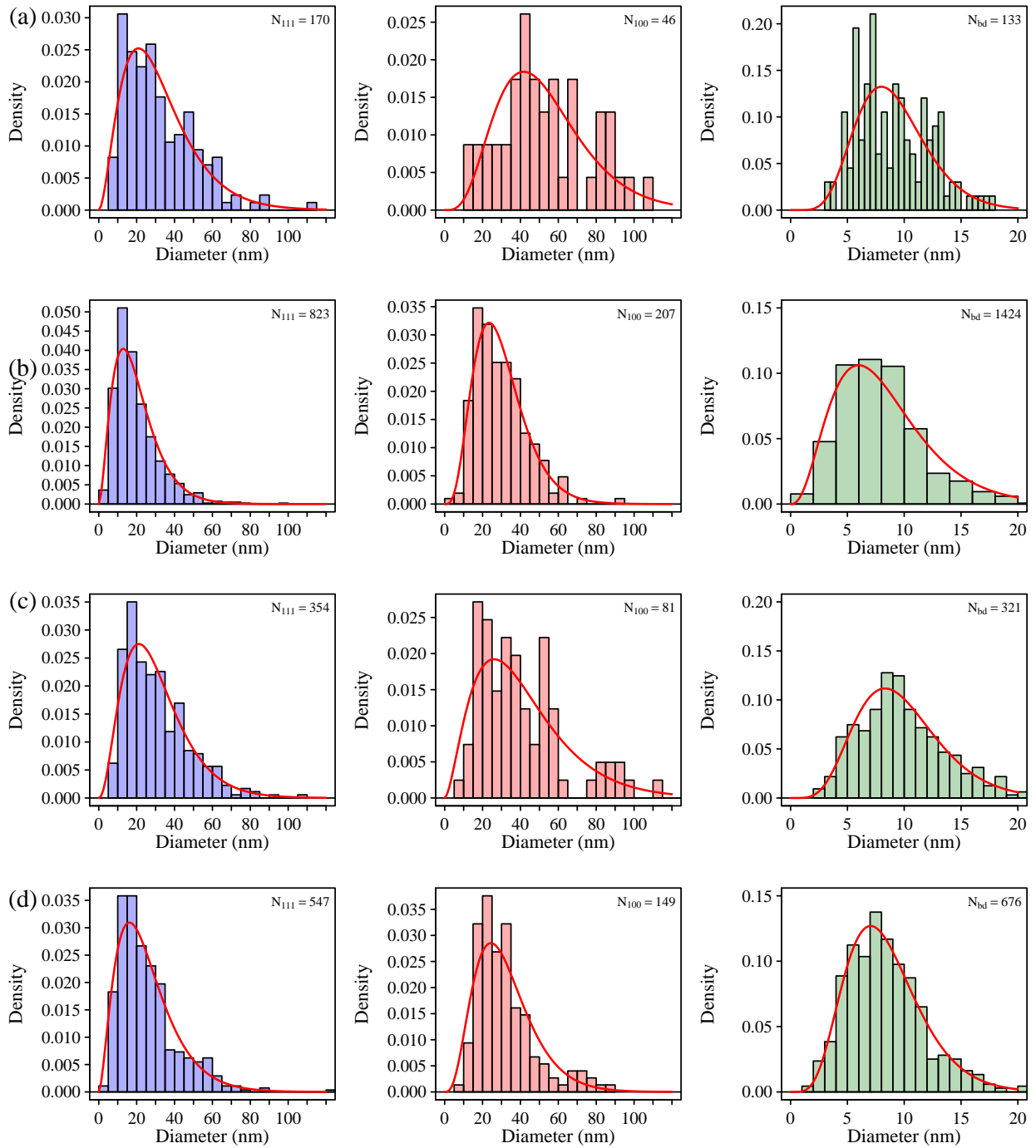
Fig. 7. Defect size distributions for $a/2\langle 111\rangle$ **loops (left-blue),** $a\langle 100\rangle$ **loops (middle-red), and black dots (right-green) for the irradiated (a) Fe-10Cr-4.8Al, (b) Fe-12Cr-4.4Al, (c) Fe-15Cr-3.9Al and (d) Fe-18Cr-2.9Al model alloys. Red lines indicate gamma distribution fit to the measured data.**

3.2 IRRADIATION ENHANCED/INDUCED $\alpha - \alpha'$ PHASE SEPARATION

3.2.1 Small angle neutron scattering (SANS) observations

The Cr-rich α' phase is notoriously difficult to image using defect contrast based electron microscopy techniques. This is due to α' being coherent with the α matrix and the weak electron scattering contrast between Fe and Cr. Therefore, advanced analytical techniques such as small angle neutron scattering (SANS) and atom probe tomography (APT) must be utilized to investigate α' formation. SANS is ideally suited to serve as a bulk analysis technique to determine the mean size, shape and number density of the α' precipitates in a Fe-based matrix. This is due to the large difference between the neutron coherent scattering lengths of Fe and Cr [31] and ability to provide structural information over the 1-200 nm scale. Due to the benefits provided by SANS, it has been historically utilized to study $\alpha - \alpha'$ phase separation in thermally aged Fe-Cr alloys [32, 33], irradiated Fe-Cr alloys [9, 34, 35] and thermally aged Fe-Cr-Al alloys [12]. Given this, it provides limited compositional information about the precipitates and therefore initial, complementary APT studies described in Section 3.2.2 have been conducted.
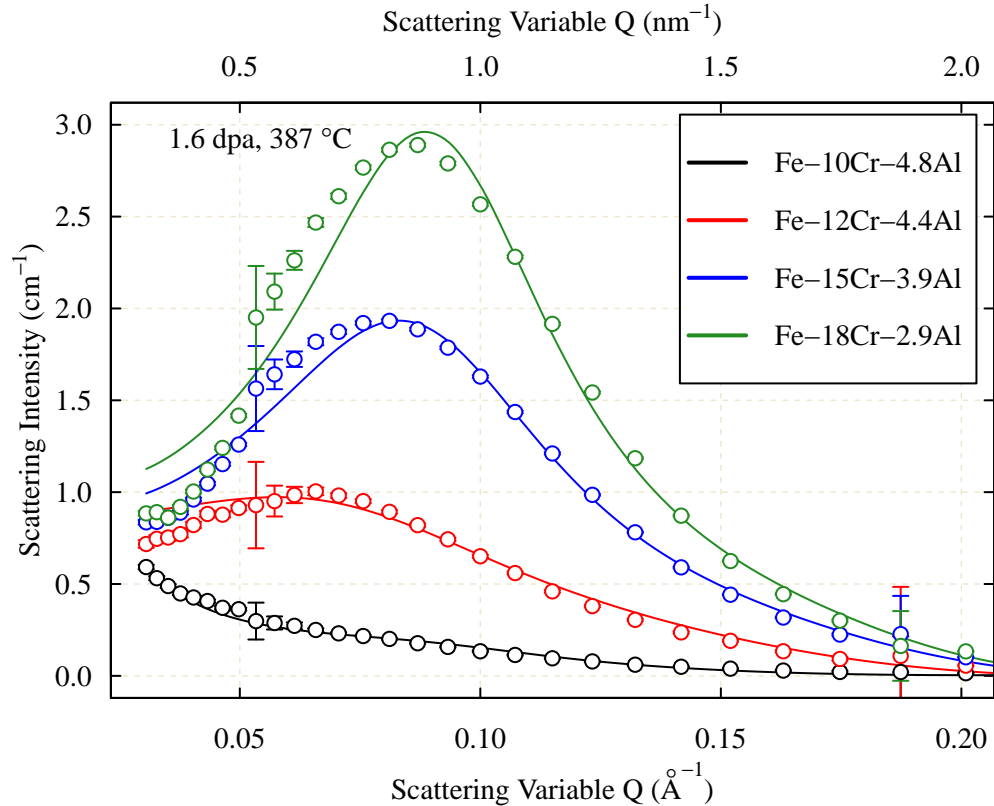
Fig. 8. Scattered intensities of irradiated Fe-Cr-Al specimens.

After irradiation, Figure 8 shows an increase of the scattering intensity above $q \geq 0.5 \; nm^{-1}$ indicative of a nanometer second phase and the intensity increases with increasing Cr content of the model Fe-Cr-Al alloys. The response of the Fe-15Cr-3.9Al and Fe-18Cr-2.9Al alloys is qualitatively similar to those seen in

thermally aged Fe-15.7Cr-4Al alloy by Messoloras *et al.* [12] or LA4Ta irradiated to 2.9 dpa at 325 °C by Mathon *et al.* [9]. Mathon *et al.* attributed the scattering intensity changes seen in reduced activation (RA) steels due to the precipitation of isolated Cr-rich α' surrounded by a spherical exclusion volume depleted in Cr. Here, the same approach was taken and the scattered intensities in Figure 8 (open symbols) were fit using a spherical exclusion model (solid lines) to extract quantitative data from the SANS signal. The relatively good fit of the model in the range of $0.5<q<2.0$ nm^{-1} to the acquired data indicates the scattering signal from the nanometer precipitates is indeed indicative of α' formation in the α matrix of the irradiated Fe-Cr-Al specimens.

Figure 9 shows the calculated size and number density of the α' precipitation based on the best fit model in Figure 8 on the irradiated Fe-Cr-Al specimens. The number density of α' precipitates increased significantly with a nearly perfect linear increase with increasing Cr content and a maximum observed at 6.8×10^{24} m^{-3} in the Fe-18Cr-2.9Al sample. The size of the precipitates were less affected by Cr composition with Fe-10Cr-4.8Al alloy being the only alloy exhibiting distinctly different average precipitate diameters compared to the other alloys investigated.
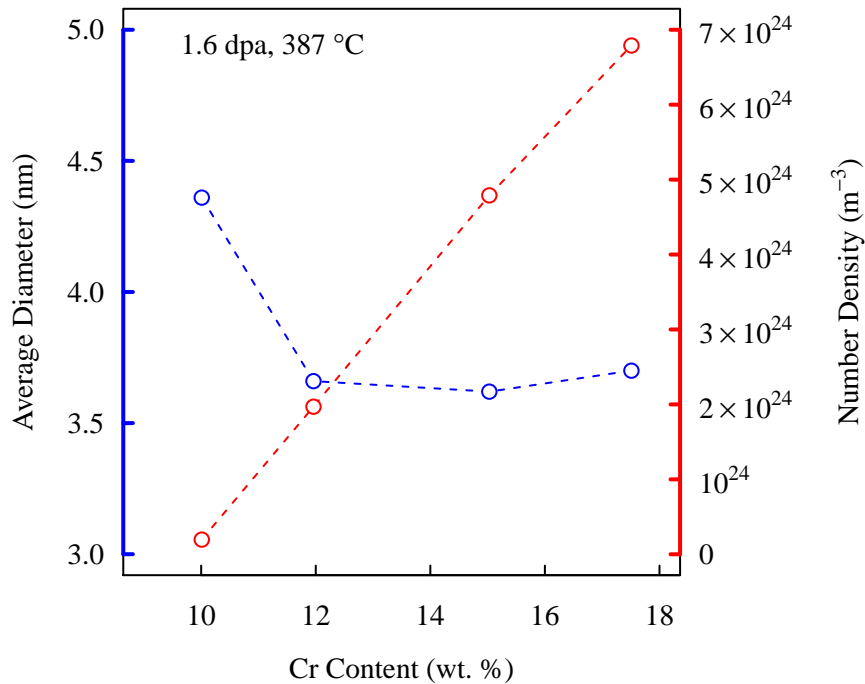
Fig. 9. Calculated size and number density of Cr-rich α' precipitates in Fe-Cr-Al samples irradiated to 1.6 dpa at 387 °C based on SANS analysis.

The results shown here are consistent with previous works on irradiated Fe-Cr and thermally aged Fe-Cr-Al alloys. Bachhav *et al.* [11] investigated a series of model Fe-Cr alloys using APT and showed the precipitation of α' to be Cr composition dependent similar to the results presented here. Bonny *et al.* [10] proposed an estimated phase diagram where precipitation of α' is expected above ~9 at. % Cr at the irradiation temperature investigated in Fe-Cr alloys. To the authors knowledge similar studies have not been conducted at the temperatures investigated here for the ternary Fe-Cr-Al phase diagram. Given this,

Kobayashi and Takasugi [14] indicated that at 475 °C $\alpha - \alpha$' phase separation is expected at the compositions investigated in this study, although Al may suppress precipitation at higher Al contents. It is probable the precipitation observed in the irradiated Fe-Cr-Al model alloys is due to an irradiation-accelerated mechanism meaning similar precipitation can be observed in neutron irradiated alloys to that of thermally aged Fe-Cr-Al alloys at higher temperatures and the results presented here support such conclusions. The precipitation of α' in all irradiated alloys suggests the solubility limit exists below 10 wt.% Cr at 387 °C for ternary Fe-Cr-Al alloys with minor Y additions. Future work would be needed to map the Fe, Cr, Al composition space to determine the solubility limit for irradiated Fe-Cr-Al alloys and the dependency on Al content proposed by Kobayashi and Takasugi.

3.2.2 Atom probe tomography (APT) observations

SANS investigations revealed formation of Cr-rich α' within the matrix of the irradiated Fe-Cr-Al alloys but did not determine if Al was partitioning to the α phase. Based on thermodynamic calculations, it is predicted Al should strongly partition to the α phase [13, 36]. Work on oxide dispersion strengthened (ODS) Fe-Cr-Al alloys show Al partitioning to the α matrix after thermal annealing with the degree of partitioning increasing with increasing annealing time [13, 36]. Here, APT was utilized to investigate if similar responses were observed in the irradiated model Fe-Cr-Al alloys. At the time of reporting, only the Fe-18Cr-2.9Al alloy has been investigated using APT. Figure 10a shows a 3-D volume of the irradiated Fe-18Cr-2.9Al alloy with a 30 at. % Cr isoconcentration surface. The sample exhibited Cr-rich clusters indicative of α'. Bachhav *et al.* [11] has indicated the analysis of α' using APT isoconcentration surfaces can be dependent on the value selected for the surface cut-off. Here, a 30 at. % Cr value was selected as it provided results similar to those observed in thermally aged Fe-Cr-Al alloys investigated in literature.

Figure 10b shows a proximity histogram across the $\alpha - \alpha$' interface in the irradiated Fe-18Cr-2.9Al. The proximity histogram reveals Al partitioning between the α and α' phases after irradiation to 1.6 dpa at 387 °C. The proximity histogram show a α' concentration of 55 at.% Cr compared to the typically quoted values of ~80 at.% Cr in literature [9, 13, 11] for α' phases in a ferritic matrix. This result suggests that under irradiation to 1.6 dpa at 387 °C the phases have not attained their equilibrium levels. If the above conclusions hold true, it would suggest the alloy is still under a phase separation regime and that further coarsening of the Cr-rich α' particles can be expected and therefore further changes in the microstructure and hence mechanical properties can be expected at higher doses. Further investigations into the high dose regime where the alloy would experience more time at temperature and increased dose is needed to determine the equilibrium or steady-state Cr concentration of the α' in irradiated model Fe-Cr-Al alloys. The solute partitioning observed on this sample also suggests the Al and Cr partitioning are coupled [36] and therefore governs the overall $\alpha - \alpha$' phase separation under irradiation.

25x25x200 nm
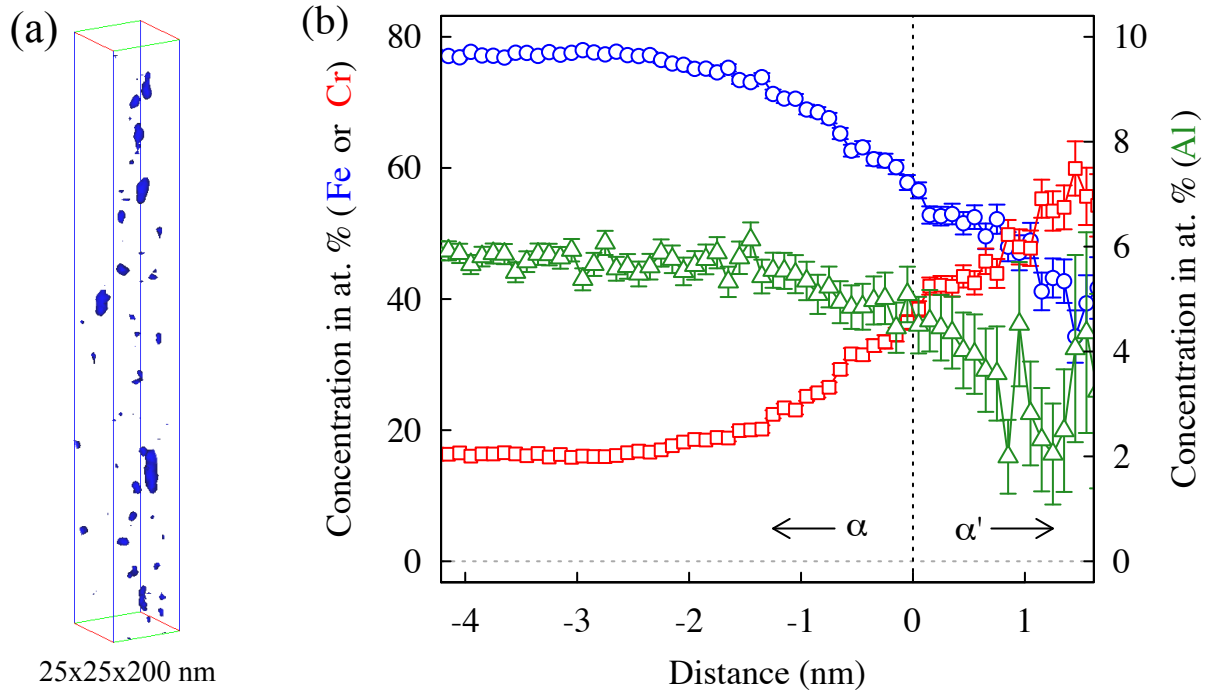
Fig. 10. APT data from irradiated Fe-18Cr-2.9Al where (a) is 30 at.% Cr isoconcentration surface showing the 3-D spatial morphology of α' and (b) shows the proximity histograms across the α − α' interfaces in the isoconcentration map.

3.3 MECHANICAL PROPERTIES

3.3.1 Experimental observations

Tensile tests were performed on each alloy before and after irradiation. The corresponding room temperature engineering stress-strain curves for the four model alloys before and after irradiation are shown in Figure 11. The stress-strain curves show radiation induced hardening with an increase in the yield and ultimate tensile strength in the Fe-12Cr-4.4Al, Fe-15Cr-3.9Al, and Fe-18Cr-2.9Al specimens although the uniform and total elongation increased or decreased depending on the specimen. The Fe-10Cr-4.9Al sample exhibited irradiation induced softening, most likely due to significant recovery of cold work compared to accumulated radiation induced defects. This will be discussed in detail in Section 3.3.2. Figure 12 summarizes the calculated yield strength, ultimate tensile strength, uniform and total elongation for all alloys before and after irradiation. It should be noted the values determined for Figures 11-12 are the result of a single tensile test and therefore no opportunity was present to develop a statistical average. This was due to the limited number of specimens available for tensile testing. Given this, Figures 11-12 shows the drastic change in the radiation induced hardening with increasing Cr content in the irradiated Fe-Cr-Al alloys. Section 3.3.2 discusses the origin of such Cr dependance with the mechanical properties based on the microstructural changes observed in the irradiated Fe-Cr-Al alloys.
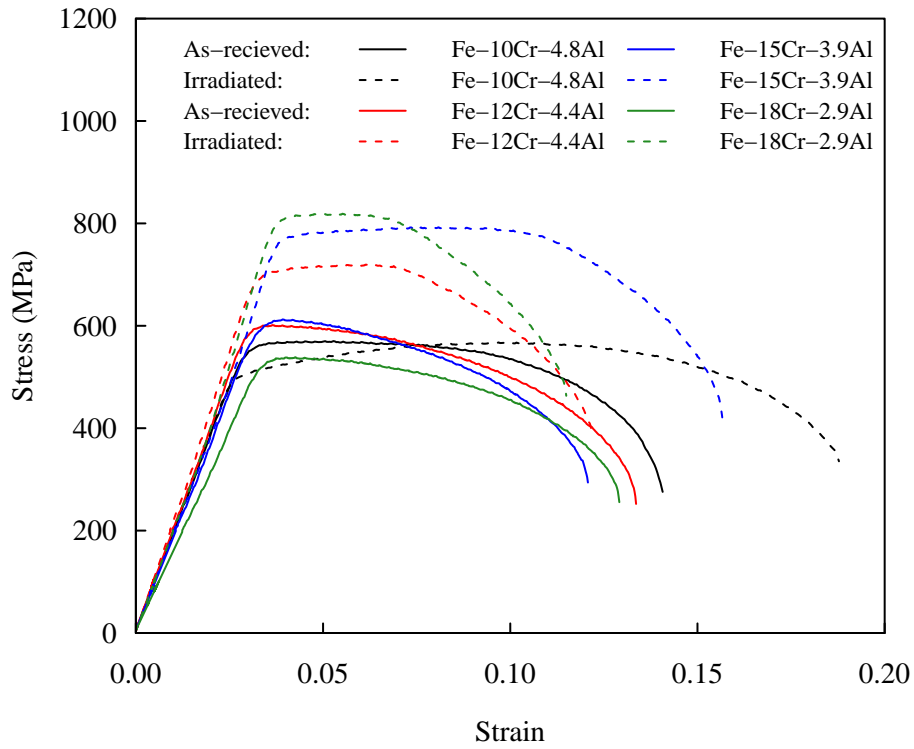
Fig. 11. Engineering stress-strain curves for the model alloys before and after irradiation.
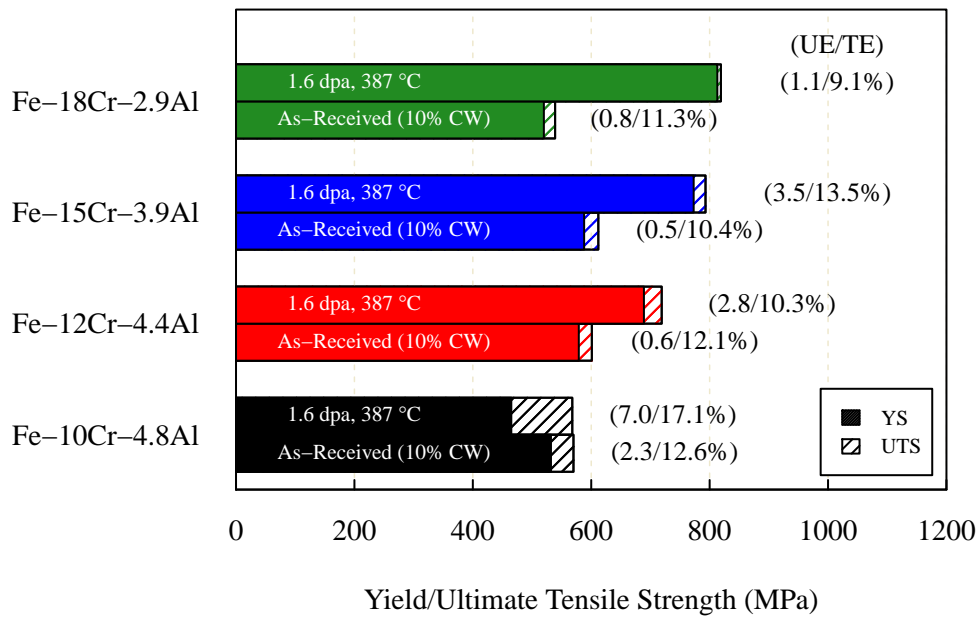
Fig. 12. Summary of mechanical properties of model alloys before and after irradiation.

3.3.2 Modeling radiation-induced hardening in Fe-Cr-Al alloys

The characterization of the irradiated Fe-Cr-Al alloys in the previous sections indicates a significant change in the microstructure due to the irradiation. Furthermore, a significant increase in the yield stress of the Fe-Cr-Al alloys was observed. Here, a hardening model is developed to couple the yield stress increase to the microstructural changes in the irradiated Fe-Cr-Al alloys. The hardening model is proposed based on the interaction of mobile dislocations with a forest of radiation induced defects. The visible radiation induced defects are those characterized in prior sections: Cr-rich α', $a/2\langle 111 \rangle$ loops, $a\langle 100 \rangle$ loops, black dots, and line dislocations or tangles/networks. A summary of the quantified values of the number density and size of each considered defect is provided in Table 2. The observed hardening is related to these defects using the well developed dispersed barrier hardening equation [37],

$$\Delta\sigma_y = M\alpha_i\mu b \sqrt{\rho_i d_i} \tag{1}$$

where $\Delta\sigma_y$ is the change in yield strength compared to the unirradiated value, μ is the shear modulus (82 GPa), M is the Taylor factor (3.06), b is the Burgers vector of $a/2\langle 111 \rangle$ dislocations interacting with the radiation induced defects during deformation (2.49x10^{-10} m), ρ_i is the number density of the ith defect, d_i is the diameter of the ith defect and α_i is the barrier strength of the ith defect interacting with the $a/2\langle 111 \rangle$ dislocations. The barrier strength can vary between zero and one. The investigated model alloys were cold-worked prior to irradiation resulting in a dislocation cell structure. The base hardening model provided in Equation 1 is only valid when the density of radiation induced defects are significantly greater than the line dislocation density induced from cold-working, an assumption not valid for this study. In-order to account for the initial dislocation network and evolution after irradiation, Equation 1 can be rewritten as [38],

$$\Delta\sigma_y = M\mu b \left(\alpha_i \sqrt{\rho_i d_i} + \alpha_d \sqrt{\rho_d} - \alpha_d \sqrt{\rho_o} \right) \tag{2}$$

where ρ_d is the resulting line dislocation density after irradiation and ρ_o is the initial dislocation density prior to irradiation from cold working of the material. In order to obtain the total yield strength change after irradiation the superposition of hardening increase for each defect type is computed. The superposition of different defects contributing to the radiation induced hardening is typically expressed either as the square root of the quadratic sum or the linear superposition of single components. Here, the linear superposition of single components was selected as it provided the most accurate modeling of the experimental results, resulting in Equation 2 being rewritten as,

$$\Delta\sigma_y = M\mu b(\alpha_{\alpha'} \sqrt{\rho_{\alpha'} \cdot d_{\alpha'}} + \alpha_{\langle 100 \rangle} \sqrt{\rho_{\langle 100 \rangle} \cdot d_{\langle 100 \rangle}}$$
$$+\alpha_{\langle 111 \rangle} \sqrt{\rho_{\langle 111 \rangle} \cdot d_{\langle 111 \rangle}} + \alpha_{black\,dots} \sqrt{\rho_{black\,dots} \cdot d_{black\,dots}} + \alpha_d (\sqrt{\rho_d} - \sqrt{\rho_o})). \tag{3}$$

Among the parameters in Equation 3, only the strength factor for each defect type is unknown based on experimental methods. The strength factor has been shown to be strongly dependent on the defect type and

20

therefore a generalized value for all defects observed can not be utilized within the model. As such, the strength factors must be determined based on empirical fitting to the experimental results in Table 2.

By linearizing Equation 3 for each alloy investigated, it can be seen that the system is underdetermined resulting in any calculation of the strength factors resulting in an inconclusive result. To overcome this issue, it is assumed the 'black dots' observed in the STEM based analysis are either $a/2\langle 111\rangle$ or $a\langle 100\rangle$ loops and due to their small nature could not be explicitly determined using the STEM based characterization technique. The calculated population of black dots is therefore partitioned into the size and number density values for the $a/2\langle 111\rangle$ and $a\langle 100\rangle$ loops based on the calculated dislocation loop anisotropy. Partitioning of the black dot data into the dislocation loop data results in the critical case where an explicit value for each strength factor can be determined by minimizing the variance between the calculated and measured yield strength values. Further characterization of other irradiation conditions for the same alloys will result in an overdetermined system and such assumptions can be neglected, but fell out of the scope of work for this report.

Table 2. Summary of radiation hardening and average size/number density of precipitates, dislocation loops and line dislocations in irradiated Fe-Cr-Al specimens.

	Fe-10Cr-4.8Al	Fe-12Cr-4.4Al	Fe-15Cr-3.9Al	Fe-18Cr-2.9Al
$\triangle\sigma_y^{irr}$ (MPa)	-67	107	185	274
ρ_o (m^{-2})	$7.2 \pm 2.2 \times 10^{13}$	$1.5 \pm 0.3 \times 10^{14}$	$1.6 \pm 0.4 \times 10^{14}$	$1.1 \pm 0.3 \times 10^{14}$
ρ_d (m^{-2})	$4.6 \pm 1.0 \times 10^{13}$	$6.3 \pm 1.6 \times 10^{13}$	$4.9 \pm 1.1 \times 10^{13}$	$6.5 \pm 3.3 \times 10^{13}$
$\rho_{\alpha'}$ (m^{-3})	1.96×10^{23}	1.97×10^{24}	4.79×10^{24}	6.79×10^{24}
$d_{\alpha'}$ (nm)	4.36	3.66	3.62	3.70
$\rho_{\langle 100\rangle}$ (m^{-3})	$4.7 \pm 2.4 \times 10^{19}$	$2.3 \pm 0.7 \times 10^{20}$	$8.5 \pm 6.0 \times 10^{19}$	$2.3 \pm 0.9 \times 10^{20}$
$d_{\langle 100\rangle}$ (nm)	52.5 ± 23.8	29.7 ± 13.7	41.1 ± 24.8	32.0 ± 15.6
$\rho_{\langle 111\rangle}$ (m^{-3})	$1.7 \pm 0.7 \times 10^{20}$	$8.9 \pm 2.8 \times 10^{20}$	$3.0 \pm 1.1 \times 10^{20}$	$8.4 \pm 3.3 \times 10^{20}$
$d_{\langle 111\rangle}$ (nm)	31.9 ± 18.7	19.8 ± 11.7	30.4 ± 16.8	25.5 ± 15.4
$\rho_{black\,dots}$ (m^{-3})	$1.4 \pm 0.4 \times 10^{20}$	$1.6 \pm 0.5 \times 10^{21}$	$3.0 \pm 0.8 \times 10^{20}$	$1.0 \pm 0.4 \times 10^{21}$
$d_{black\,dots}$ (nm)	9.1 ± 3.2	8.2 ± 4.3	9.8 ± 3.8	8.4 ± 3.4

The resulting barrier strength factors for each defect was computed using the inputs from Table 2 resulting in $\alpha_{\alpha'} = 0.043$, $\alpha_{\langle 100\rangle} = 0.325$, $\alpha_{\langle 111\rangle} = 0.079$, and $\alpha_d = 0.687$. These barrier strength factors were calculated based on finding the best fit to Equation 3 and taking into account the uncertainty levels provided in Table 2. It should be noted that the uncertainty in the measured yield strength changes was not accounted for, but some uncertainty is expected. Further tensile tests would be needed to determine the uncertainty bounds in the experimentally determined changes in yield strength after irradiation.

The resulting model assumes the average strength of each defect type based on the average size of the defects observed. Recent work in austenitic and pure iron alloys indicate the barrier strength can be dependent on the defect size [39, 40]; future work will consider the calculated size distributions into the radiation induced hardening model. Finally, the model presented here only takes into account the visible, or those defects which were resolvable using STEM or SANS. STEM based techniques have a finite lower limit on resolvable defects and as such it can be assumed defects below this limit were not resolved in this study. These 'non-visible' defects, such as small solute clusters or nano-voids, can also contribute to the radiation induced hardening response. The effect of these non-visible defects were not included in the

current analysis, and thus some error is intrinsic in the values given for the barrier strength values. Given the errors associated with the experimental analysis and simplifications assumed in the model, the model presented here serves only as a first-order approximation of the system and some variability is expected although it does provide insight into the correlation between microstructural and mechanical changes in the model Fe-Cr-Al alloys.

Lucas [41] indicated three different regimes for defect types: 1) weak barrier with $\alpha<0.25$ such as small loops or black dots, 2) intermediate barriers with $0.33<\alpha<0.45$ such as larger dislocation loops, and strong barriers with $\alpha\approx1$ such as large precipitates. Hence, the α' precipitates with an α of 0.043 represent a relatively weak barrier and in small number densities do not significantly contribute to the hardening. In contrast, the dislocation loops, of both types, represent intermediate barriers to dislocation motion and can significantly contribute to the hardening. It is of interest that the sessile $a\langle100\rangle$ loops exhibit, on average, are a stronger barrier to motion than glissile $a/2\langle111\rangle$ loops. The difference in the strength of the two dislocation types is most likely due to their sessile and glissile nature under deformation. It also suggests that dislocation loop anisotropy can have a significant impact on the hardening of Fe-Cr-Al alloys during and after irradiation.

Based on the empirically determined barrier strength of each defect type, the contributions to the experimentally determined hardening can be computed, as seen in Figure 13. Several important features of the system can be derived from Figure 13. The first is that although α' precipitates are the weakest barrier in the irradiated model Fe-Cr-Al alloys, the large number density at high Cr contents (>12 wt.% Cr) leads to significant contributions in the hardening response of the alloys. Such interplay between the hardening effect and number density change as a function of Cr content drives the Cr composition hardening response seen in Figure 12. Based on this conclusion, it becomes clear the Cr content of the irradiated Fe-Cr-Al alloys must be reduced to limit radiation induced hardening from α' precipitates. The second is the dislocation loops are intermediate strength barriers but their influence on hardening is limited due to their low density. Last, the line dislocations present the strongest barriers to dislocation motion and based on the hardening contributions for α' precipitates and dislocation loops, radiation induced softening can be observed, such as was observed in the Fe-10Cr-2.9Al alloy.
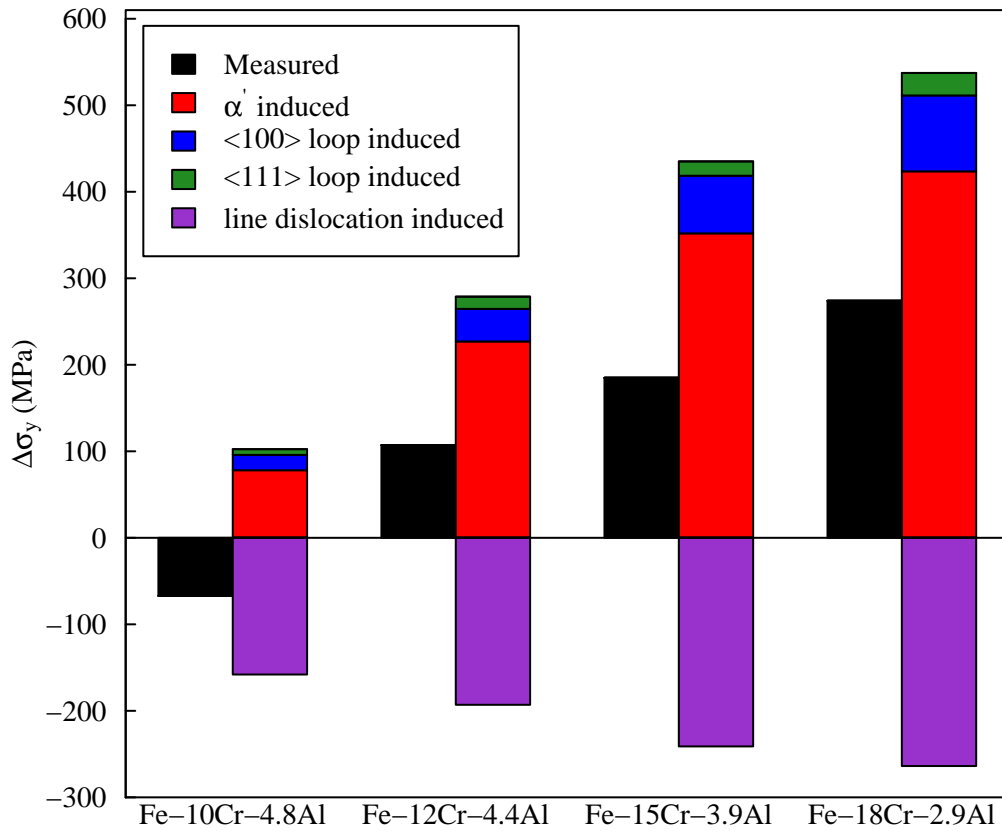
Fig. 13. Radiation induced hardening contributions due to different measured defects based on developed radiation hardening model.

4. CONCLUSIONS

Fe-Cr-Al alloys were fabricated, irradiated in the HFIR, and characterized to determine the stability of Fe-Cr-Al alloys in the presence of neutrons. The visible radiation induced microstructure consisted of Cr-rich α' precipitates, 'black dots', line dislocations, $a/2\langle111\rangle$ and a$\langle100\rangle$ dislocation loops. No voids/bubbles were observed in any specimens investigated. These microstructural features impacted the mechanical properties with radiation induced hardening observed and highest in the Fe-18Cr-2.9Al alloy. It was demonstrated a dispersed barrier hardening model could be developed to link the change in microstructure to the change in mechanical properties. Based on such analysis the following statements can be made:

- Cr-rich α' precipitates are a weak barrier to dislocation motion, but their contribution to radiation hardening can become significant with sufficiently high number densities.

- Dislocation loops contribute to the hardening response with the sessile/glissile nature of the defect loops controlling their barrier strength. It is proposed sessile, $a\langle100\rangle$ loops are stronger barriers to dislocation motion than $a/2\langle111\rangle$ loops.

- The strong dependence on Cr composition is directly related to the mechanisms controlling the $\alpha - \alpha$' phase separation. The increase in number density of α' precipitates is linearly related to a change in Cr composition and at high Cr contents (>12 wt.% Cr) the α' precipitates dominate the hardening response in Fe-Cr-Al alloys.

Based on these results it can be concluded the Cr content of Fe-Cr-Al alloys should be minimized to reduce α' precipitation under the presence of neutron irradiation.

5. REFERENCES

[1] M. Moalem and D.R. Olander. Oxidation of Zircaloy by steam. *Journal of Nuclear Materials*, 182:170–194, 1991. 1.

[2] B.A. Pint, K.A. Terrani, M.P. Brady, T. Cheng, J.R. Keiser, et al. High temperature oxidation of fuel cladding candidate materials in steam-hydrogen environments. *Journal of Nuclear Materials*, 440:420–427, 2013. 1.

[3] M.T. Farmer, L. Leibowitz, K.A. Terrani, and K.R. Robb. Scoping assessments of ATF impact on late-stage accident progression including molten core-concrete interaction. *Journal of Nuclear Materials*, 448(1-3):534–540, 2014. 1.

[4] K.A. Terrani, S.J. Zinkle, and L.L. Snead. Advanced oxidation-resistant iron-based alloys for lwr fuel caldding. *Journal of Nuclear Materials*, 448(1-3):420–435, 2013. 1.

[5] Y. Yamamoto, Y. Yang, K.G. Field, K.A. Terrani, B.A. Pint, and L.L. Snead. M3FT-13OR0202291: Development of improved ATF engineering alloy - CALPHAD calculations and initial billet production. Technical report, Oak Ridge National Laboratory, 2014. 1.

[6] K.G. Field, M.N. Gussev, Y. Yamamoto, and L.L. Snead. Deformation behavior of laser welds in high temperature oxidation resistant Fe-Cr-Al alloys for fuel cladding applications. *Journal of Nuclear Materials*, 454(1-3):352–358, 2014. 1.

[7] S. Zinkle and J. Busby. Structural materials for fission and fusion energy. *Materials Today*, 12(11):12–19, 2009. 1., 3.1.1

[8] D. Terentyev, G. Bonny, C. Domain, G. Monnet, L. Malerba, et al. Mechanisms of radiation strengthening in Fe-Cr alloys as revealed by atomistic studies. *Journal of Nuclear Materials*, 442(1-3):470–485, 2013. 1.

[9] M.H. Mathon, Y. De Carlan, G. Geoffroy, X. Averty, A. Alamo, and C.H. De Novion. A SANS investigation of the irradiation enhanced α-α' phases separation in 7-12 Cr martensitic steels. *Journal of Nuclear Materials*, 312(2-3):236–248, 2003. 1., 3.2.1, 3.2.1, 3.2.2

[10] G. Bonny, D. Terentyev, and L. Malerba. On the α-α' miscibility gap of Fe-Cr alloys. *Scripta Materialia*, 59:1193–1196, 2008. 1., 3.2.1

[11] M. Bachhav, G.R. Odette, and E.A. Marquis. α' precipitation in neutron-irradiated Fe-Cr alloys. *Scripta Materialia*, 74:48–51, 2013. 1., 3.2.1, 3.2.2

[12] S. Messoloras, B.C. Pike, R.J. Steward, and C.G. Windsor. Precipitation in iron-chromium-aluminium alloys. *Metal Science*, 18:311–321, 1984. 1., 3.2.1, 3.2.1

[13] C. Capdevila, M.K. Miller, and K.F. Russell. Aluminum partitioning during phase separation in Fe-20Cr-6Al ODS alloy. *Journal of Materials Science*, 43:3889–3893, 2008. 1., 2.6, 3.2.2

[14] S. Kobayashi and T. Takasugi. Mapping of 475C embrittlement in ferritic Fe-Cr-Al alloys. *Scripta Materialia*, 63(11):1104–1107, 2010. 1., 3.2.1

[15] B.A. Pint. Experimental observations in support of the dynamic-segregation theory to explain the reactive-element effect. *Oxidation of Metals*, 45(1/2):1–37, 1995. 2.1

[16] B.A. Pint. Optimization of reactive-element additions to improve oxidation performance of alumina-forming alloys. *Journal of American Ceramic Society*, 86(4):686–695, 2003. 2.1

[17] K.G. Field, L.M. Barnard, C.M. Parish, J.T. Busby, D.D. Morgran, and T.R. Allen. Dependence on grain boundary structure of radiation induced segregation in a 9wt. Cr model ferritic/martensitic steel. *Journal of Nuclear Materials*, 435(1-3):172–180, 2013. 2.4

[18] D.B. Williams and C.B. Carter. *Transmission Electron Microscopy*. Plenum Press, 1996. 2.4

[19] G.D. Wignall, K.C. Littrell, W.T. Heller, Y.B. Melnichenko, K.M. Bailey, G.W. Lynn, D.A. Myles, V.S. Urban, M.V. Buchanan, D.L. Selby, and P.D. Butler. The 40 m general purpose small-angle neutron scattering instrument at Oak Ridge National Laboratory. *Journal of Applied Crystallography*, 45:1–9, 2012. 2.6

[20] B. Yao, D.J. Edwards, and R.J. Kurtz. TEM characterization of dislocation loops in irradiated bcc Fe-based steels. *Journal of Nuclear Materials*, 434(1-3):402–410, 2013. 3.1.1

[21] S.I. Porollo, A.M. Dvoriashin, A.N. Vorobyev, and Yu.V. Konobeev. The microstructure and tensile properties of Fe-Cr alloys after neutron irradiation at 400C to 5.5-7.1 dpa. *Journal of Nuclear Materials*, 256:247–253, 1998. 3.1.1

[22] S.L. Dudrev, R. Bullough, and P.M. Derlet. Effect of the a-g phase transition on the stability of dislocation loops in bcc iron. *Physical Review Letters*, 100:1–4, 2008. 3.1.1

[23] S.P. Fitzgerald and Z. Yao. Shape of prismatic dislocation loops in anisotropic α-Fe. *Philosophical Magazine Letters*, 89(9):581–588, 2009. 3.1.1

[24] A. Amali, P. Rez, and J.M. Cowley. High angle annular dark field imaging of stacking faults. *Micron*, 28(2):89–94, 1997. 3.1.1

[25] J.M. Cowley and Y. Huang. De-channelling contrast in annular dark-field STEM. *Ultramicroscopy*, 40:171–180, 1992. 3.1.1

[26] C.J. Humphreys. Fundamental concepts of STEM imaging. *Ultramicroscopy*, 7:7–12, 1981. 3.1.1

[27] D.D. Perovic, C.J. Rossouw, and A. Howie. Imaging elastic strains in high-angle annular dark field scanning transmission electron microscopy. *Ultramicroscopy*, pages 353–359, 1993. 3.1.1

[28] P.J. Phillips, M.C. Brandes, M.J. Mills, and M. De Graef. Diffraction contrast STEM of dislocations: imaging and simulations. *Ultramicroscopy*, 111(9-10):1483–1487, 2011. 3.1.1

[29] E.A. Little and D.A. Stow. Void-swelling in irons and ferritic steels: II. An experimental survey of materials irradiated in a fast reactor. *Journal of Nuclear Materials*, 87(1):25–39, 1979. 3.1.3

[30] H.H. Jin. Fabrication of a TEM sample of ion-irradiated material using focused ion beam microprocessing and low-energy Ar ion milling. *Journal of Electron Microscopy*, 59(6):463–468, 2010. 3.1.3

[31] M. Furusaka, Y. Ishikawa, S. Yamaguchi, and Y. Fujino. Spinodal decomposition in Fe-Cr alloys studied by small angle neutron scattering. *Physica*, 120B:383–386, 1983. 3.2.1

[32] S. Katano and M. Iizumi. Crossover phenomenon in dynamical scaling of phase separation in Fe-Cr alloy. *Physical Review Letters*, 52(10):835–838, 1984. 3.2.1

[33] F. Bley. Neutron small-angle scattering study of unmixing in Fe-Cr alloys. *Acta Metallurgica et Materialia*, 40(7):1505–1517, 1992. 3.2.1

[34] F. Bergner, A. Ulbricht, and C. Heintze. Estimation of the solubility limit of Cr in Fe at 300C from small angle neutron scattering in neutron-irradiated fe-cr alloys. *Scripta Materialia*, 61(11):1060–1063, 2009. 3.2.1

[35] C. Heintze, F. Bergner, A. Ulbricht, and H. Eckerlebe. The microstructure of neutron-irradiated Fe-Cr alloys: A small-angle neutron scattering study. *Journal of Nuclear Materials*, 409:106–111, 2011. 3.2.1

[36] C. Capdevila, M.K. Miller, and J. Chao. Phase separation kinetics in a Fe-Cr-Al alloy. *Acta Meterialia*, 60:4673–4684, 2012. 3.2.2

[37] D. McLean. *Mechanical Properties of Metals*. Wiley, New York, 1962. 3.3.2

[38] C. Pokor, Y. Brechet, P. Dubuisson, J.-P. Massoud, and X. Averty. Irradiation damage in 304 and 316 stainless steels: experimental investigation and modeling. Part ii: Irradiation induced hardening. *Journal of Nuclear Materials*, 326:30–37, 2004. 3.3.2

[39] L. Tan and J. Busby. Formulating the strength factor a for improved predictibility of radiation hardening. *In-submission: Journal of Nuclear Materials*, 2014. 3.3.2

[40] X. Hu, D. Hu, T.S. Byun, and B.D. Wirth. Modeling of irradiation hardening of iron after low-dose and low-temperature neutron irradiation. *Modeling Simul. Materi. Sci. Eng.*, 22, 2014. 3.3.2

[41] G.E. Lucas. The evolution of mechanical property change in irradiated austenitic stainless steels. *Journal of Nuclear Materials*, 206(2-3):287–305, 1993. 3.3.2